Stress, strain, neutron transport and radiation effects in a full fusion tokamak device: a virtual MAST-U study

Luca Reali[1,*], *William M. E.* Ellis[1,**], *Ander* Gray[1,***], *Max* Boleininger[1,****], *Andrew* Davis[1,†], *Helen M.* Brooks[1,‡], *Ioannis* Katramados[1,§], *Andrew J.* Thornton[1,¶], *James* Buchanan[1,‖], and *Sergei L.* Dudarev[1,**]

[1]UK Atomic Energy Authority, Culham Campus, Oxfordshire OX14 3DB, United Kingdom

Abstract. A finite-element method (FEM) model for the Mega-Ampere Spherical Tokamak - Upgrade (MAST-U) fusion tokamak has been developed to evaluate stress and deformations in the full device structure and to assess the stability of the whole tokamak with respect to its simulated exposure to an artificial level of neutron irradiation. Here, we use MAST-U as a proxy for a fusion power plant to explore the level of fidelity made possible by modern supercomputing systems. Gravity and atmospheric pressure were used to test the high-resolution FEM model, involving in excess of 122 million elements. Taking the MAST-U fusion plasma as a neutron source, we perform full-scale neutron transport calculations to quantify spatial variations in the neutron flux and assess the neutron radiation exposure across the structure. This is a first step towards applying recently developed multiscale computational tools to evaluate the spectrum of stress in the tokamak, identifying the location of stress concentrations as well as their magnitude. This study provides an example of full fusion device neutronics and FEM simulations which are enabling UKAEA to define computational requirements for modelling a whole fusion power plant as well as for specifying operating conditions for the relevant materials.

1 Introduction

Historically, the evolution of fusion devices has been driven by empirical scaling laws of plasma confinement, reflected in the successive heuristic construction of several generations of tokamaks as well as other fusion systems [1]. The notion of Integrated Tokamak modelling still refers solely to plasma dynamics [2], with structural engineering models primarily exploring individual device components, for example superconducting magnets, divertor targets, and breeding blanket modules [3]. Fusion reactor structure optimisation, reflecting the operating conditions in the whole device and being conceptually similar to the optimisation of electromagnetic coils in a fusion stellarator [4], has not yet been attempted. Studies of individual reactor components, while offering insight into their operation and performance, do not provide the means for defining the loading conditions on these components. Specifying

[*]e-mail: Luca.Reali@ukaea.uk (corresponding)
[**]e-mail: William.Ellis@ukaea.uk
[***]e-mail: Ander.Gray@ukaea.uk
[****]e-mail: Max.Boleininger@ukaea.uk
[†]e-mail: Andrew.Davis@ukaea.uk
[‡]e-mail: Helen.Brooks@ukaea.uk
[§]e-mail: Ioannis.Katramados@ukaea.uk
[¶]e-mail: Andrew.Thornton@ukaea.uk
[‖]e-mail: James.Buchanan@ukaea.uk
[**]e-mail: Sergei.Dudarev@ukaea.uk

the loading conditions requires the treatment of interaction between components in the entire device, and hence implies the availability of a model for a full operating reactor. Similarly, a full reactor model is needed for defining the operating conditions for materials, for example the range of operating temperature, stress, radiation dose and dose rate, magnetic forces, the rates of radiation-assisted chemical permeation and erosion, since these parameters are established self-consistently through the operation of the fusion device. A quantitative definition of a representative range of operating conditions for materials in a power plant also implies the assessment of the *frequency of occurrence* of these conditions, since some conditions occur in a reactor structure more often and hence warrant greater attention in the context of a materials testing programme. The extreme nature of operating conditions for materials in a fusion power plant also implies a high rate of materials ageing, an issue well recognised in nuclear fission [5].

2 From CAD to FEM representation of the tokamak structure

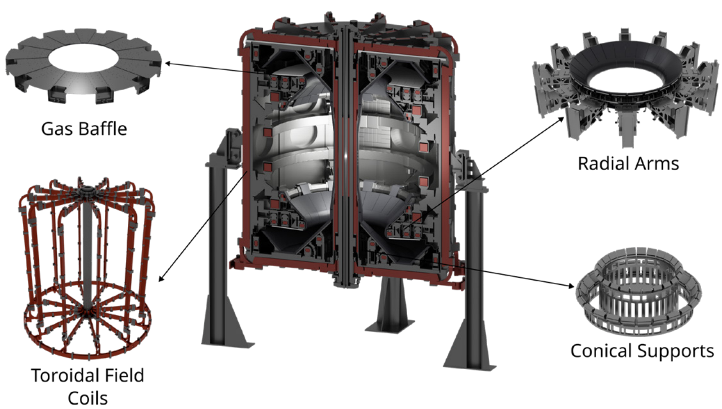

Figure 1. The CAD assembly of the MAST-U model with annotations showing the placement of the radial arms (or main support brackets), conical supports, gas baffle and toroidal field coils.

Below, we explore the structural mechanics aspect of a full tokamak model, focusing on its consistency as well as on the complexity of the computational representation of the device. To provide an example of application of the simulation methodology, we develop a model for the real large-scale tokamak device MAST-U operating at the Culham Campus of UKAEA.

After the Mega-Ampere Spherical Tokamak (MAST) operated from 1999-2013 [6], the upgraded machine MAST-U [7, 8] began operations in 2020. The vacuum vessel of the device is made of non-magnetic 304S62 austenitic stainless steel (SS), with copper magnets and a carbon-tiled double divertor. The vacuum vessel cylinder is suspended on four supporting legs attached to a concrete foundation.

Fig. 1 illustrates the structure of the MAST-U tokamak and outlines the logic of the study below. We start from a CAD (computer-aided design) representation of the device previously used for performing neutron transport calculations. This model had geometrically small details expunged which do not significantly impact neutron transport, but are critical for realistic mechanical analysis to ensure proper mechanical connection of components to the tokamak structure. Using a detailed reference CAD model, known as the Digital Mock Up (DMU) for MAST-U at UKAEA, the requisite components are modelled and implemented into the complete analysis model. Picking out the necessary components from the reference geometry acts as a form of manual de-featuring, as it forces prioritisation of components and helps avoid modelling excessive detail such as those of small size like nuts and bolts. This process helps ensure that the final geometry is tractable by the meshing preprocessor Coreform Cubit [9]. Cubit was used due to its prevalence in mesh preparation for advanced modelling and simulation applications. Prior to meshing, the model must undergo a process known as imprinting and merging (called shared topology in some software). For the added components to provide proper mechanical support, coincident surfaces must be merged together to ensure the contiguity of mesh elements across shared boundaries. Surfaces can only be merged if they have like topology, which is achieved via imprinting, a process where curves from one surface are projected on to another.

The final CAD model features 3938 individual component volumes and 11,477 merged surfaces. The tetrahedral mesh representation of this model is generated in Coreform Cubit and then loaded into the finite element method (FEM) solver MOOSE [10], supplemented by material properties and boundary conditions. Simulation results are validated using the available measurements taken on the physical device. Effects of neutron irradiation on materials are modelled using the eigenstrain formalism [11, 12]. Potential sources of uncertainties are established and analysed, contributing to the uncertainty quantification (UQ) of the model.

Fig. 2 illustrates the 122M tetrahedral element FEM model for the tokamak device. The figure shows both the full scale view of the device, and the cross-sectional magnified view of the FEM mesh, highlighting the high level of structural complexity of the device where plasma confinement is achieved through the combined operation of poloidal and toroidal magnetic coils, and where currents in the magnets are controlled independently to vary the

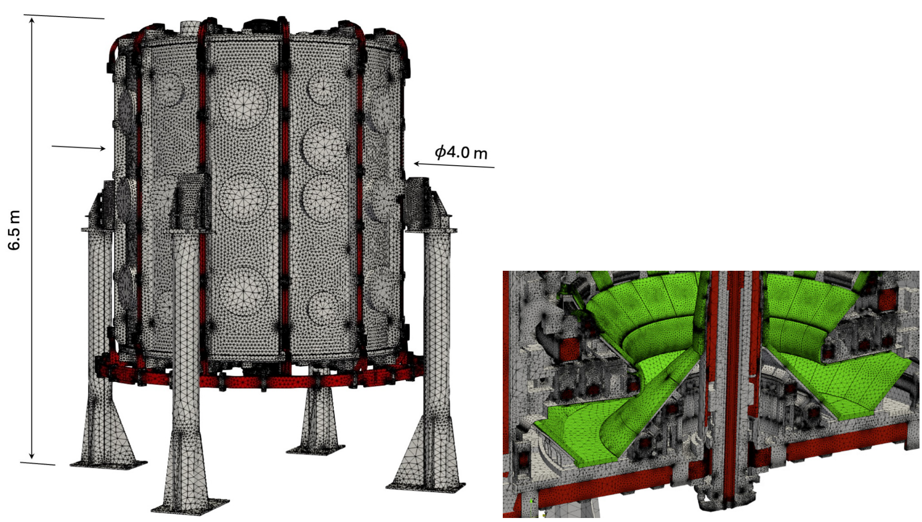

Figure 2. Schematic view of the FEM representation of the MAST-U tokamak. The full FEM model of the tokamak structure, developed in this study, involves approximately 122 million individual tetrahedral elements. The total height of the device, including the legs supporting the cylinder, is about 6.5 metres. The cylindrical vacuum vessel has the internal radius of 2.0 m and the internal height of 4.4 m. The thickness of steel walls of the vacuum vessel is approximately 20 mm. The volume of the fusion plasma in the MAST-U tokamak is 8 m^3. The magnified cross-sectional view of the FEM mesh highlights the current-carrying copper magnetic coils, red, and carbon divertor tiles, green.

configuration of the plasma. While the position of magnets is defined with high precision in a static CAD model, dynamic FEM simulations show that magnetic coils mechanically deform and vibrate in response to applied external mechanical loads, including for example plasma disruptions, resulting in fluctuations of the magnetic field confining the plasma. This FEM model is used below to assess the distributions of stress and deformations in the loaded tokamak structure, and in future developments will be instrumental to assess stress, strain and deformations resulting from neutron exposure.

3 Full tokamak-scale neutron transport simulations

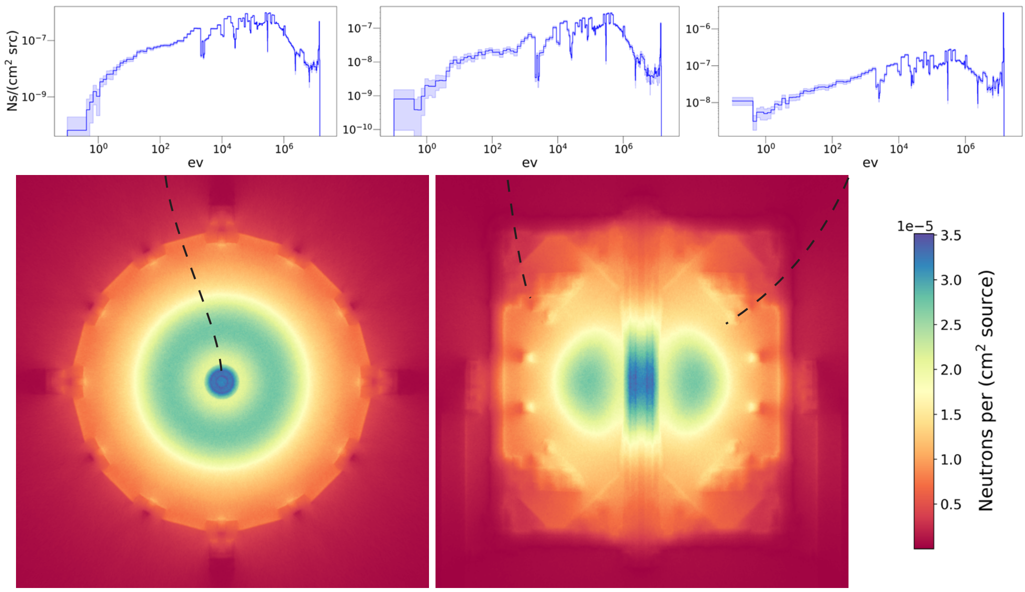

Figure 3. Predicted neutron flux field in the two planar cross-sections of the MAST-U tokamak structure: (left) top-down view, and (right) side view. The plots show the flux in the units of neutrons per square cm per produced source neutron. Additionally shown are three examples of computed detailed neutron flux spectra at (left) the central solenoid, (centre) a poloidal field coil, and (right) a graphite magnet shielding, with dashed lines indicating the approximate locations from where the neutron spectra were taken.

This section briefly describes how the plasma neutron source is defined and how neutrons are transported through the tokamak structure. The effects of interaction of neutrons with materials, resulting in the energy release and the production of defects, are summarised in the next section of the study. Although MAST-U ignites a deuterium-deuterium (D-D) plasma, we simulate here the impact of a deuterium-tritium (D-T) plasma on the machine.

The approximated nuclear description of the MAST-U tokamak has three materials present, 304 Stainless Steel, Pure Copper for the magnets and Graphite for the plasma facing carbon tiles. Inside the poloidal field coils there is a thin layer of plastic epoxy resin, providing insulation for the copper conductor, but this was not preserved in the mechanical model as an approximated homogenised description of the conducting structures was taken. Future work using this model will likely include a more detailed description of the conductor for the purposes of calculating the vacuum field. The neutron source is that taken from Ref. [13]

with parameters selected that are typical of a MAST-U discharge, with the exception that the neutrons born are those born from D-T fusion i.e. 14.08 MeV with a FWHM of 136.6 KeV. The OpenMC Monte Carlo code [14] version 0.14.0 was used to run the neutron transport simulations, using the DAGMC extension to allow CAD geometries to be used, further the Double Down [15] interface to DAGMC was used to reduce runtime to that equivalent of a native model. All nuclear data were defined as those coming from the JEFF-3.3 library [16], and the code was run for 10×10^7 histories per batch with 20 total batches. Fig. 3 shows the predicted neutron flux field in two planar cross-section views, from the neutron data transported directly on the meshed CAD geometry, along with several examples of the energy resolved flux spectra. The vitamin-J 175 energy group structure was used to tally the energy resolved spectra.

4 Effects of neutron irradiation on materials

As was noted in the preceding section, fusion D-T reactions in the plasma produce highly energetic neutrons. Exposure of materials to irradiation, including neutrons, is quantified using the notion of the dose, expressed in dimensionless displacement per atom (dpa) units. The dpa value states how many times, on average, an atom has been ballistically displaced by a collision with a high-energy particle over the entire duration of exposure. One of the effects of exposure to neutrons is the production of point defects, namely self-interstitial atoms and vacancies. The other effect is the generation of γ-quanta [17]. Collision cascades initiated by neutron impacts on atomic nuclei, and the resulting defect microstructure, can be fairly accurately modelled using molecular dynamics. Fig. 4 compares microstructures forming in tungsten exposed to 0.03 and 0.3 dpa [18, 19].

On the macroscopic scale, exposure to irradiation is characterised by notable spatial variations. For example, neutron flux decreases rapidly away from the plasma. Moreover, different materials have different neutron attenuation powers, and this self-consistently affects the magnitude of the *local* neutron exposure, giving rise to gradients in the rate with which defects

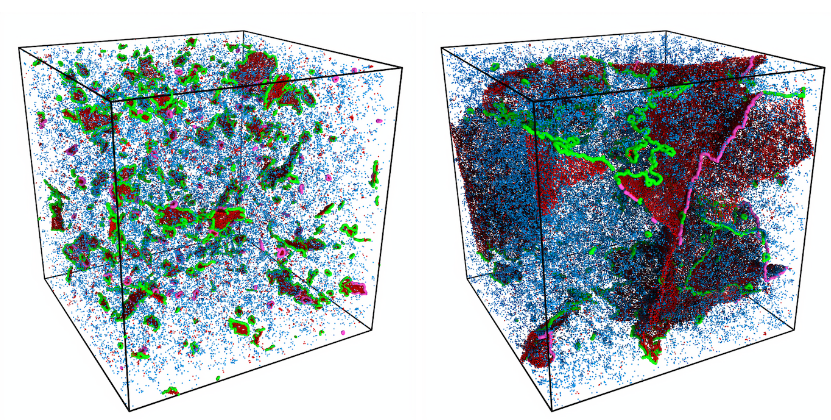

Figure 4. Comparison of defect microstructures forming in tungsten following its exposure to a relatively low and a relatively high radiation dose. The microstructure shown on the left corresponds to 0.03 dpa exposure; the microstructure shown on the right corresponds to 0.3 dpa; simulations involved no applied stress. Vacancy defects remain randomly distributed in the material in both cases; self-interstitial defects exhibit a strong tendency to clustering, forming dislocation loops and, at higher doses, extended dislocation networks.

are generated in a material, resulting in the gradients in the swelling rate pronounced on the macroscopic scale of reactor components. Furthermore, irradiation gives rise to microstructural fluctuations illustrated in Fig. 4, stemming from defect coalescence and interactions, and also from radiation-induced precipitation and segregation of solute elements in alloys. Swelling gradients give rise to internal body forces developing in the bulk of the materials; these body forces produce significant macroscopic stress and deformations [12].

To illustrate the occurrence of stresses generated by a spatially fluctuating radiation exposure, we consider a cylinder, shown in Fig. 5, with the size comparable to that of the vacuum vessel of MAST-U. Inner and outer radii of the cylinder are chosen at 1.5 and 1.75 m; the height is 4 m. A linear elastic model for material was used, with properties similar to those of conventional structural steel with the shear modulus of $\mu = 80$ GPa and Poisson's ratio of $\nu = 0.3$. The radiation-induced swelling profile was generated by superimposing a slowly spatially varying swelling and rapidly varying fluctuations taken in the form of sinusoidal wave variations with wavelengths on the centimetre scale. This qualitative example illustrates the combined effect of average neutron exposure and local spatial variations of the neutron flux resulting from the complexity of the fusion device structure, containing magnets, ports, brackets, shown in Fig. 2. These components shield the vacuum vessel from the neutrons generated by the plasma. The FEM solution for stress and deformations reflects the spatial variation of the resulting defect eigenstrain [11, 12]. The spatially varying von Mises stress stemming from the spatially varying eigenstrain is illustrated in Fig. 5. Detailed analysis shows that the internal hydrostatic pressure in the structure, related to the trace of the elastic stress tensor as $p(\mathbf{r}) = -\frac{1}{3}\sigma_{ii}(\mathbf{r})$ is proportional to the local swelling $\omega(\mathbf{r})$ via $p(\mathbf{r}) \sim \mu[\omega(\mathbf{r}) - \overline{\omega(\mathbf{r})}]$, where $\overline{\omega(\mathbf{r})}$ is the swelling averaged over the volume of a traction-free component and μ is the shear modulus [12]. Given that the characteristic scale of the shear

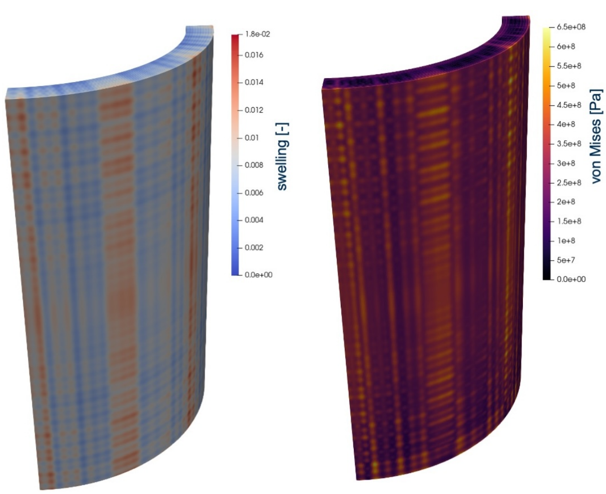

Figure 5. A cylindrical shell subjected to spatially varying radiation exposure, illustrating the effect of spatially fluctuating eigenstrains taken in the form $\omega_{ij}(\mathbf{r}) = \frac{1}{3}\delta_{ij}\omega(\mathbf{r})$, where function $\omega(\mathbf{r})$ is referred to as swelling. One eigth of the cylinder wall is shown to exploit symmetries. The eigenstrain shown on the left is a superposition of short- and long-wavelength oscillations, with the peak value of about 1.5-2%. This generates stress fields with the same spatial pattern illustrated on the right in the form of the distribution of the von Mises stress invariant. The shear modulus of steel is $\mu = 80$ GPa and the magnitude of stress in the cylindrical structure reaches ~650 MPa.

modulus of a steel or a tungsten alloy is of order 100 GPa, spatial fluctuations of swelling on the 0.1% scale generate stress fluctuations of order 100 MPa.

5 Full tokamak device structural analysis: macroscopic effects of gravity and atmospheric pressure

Stress in the structure of a tokamak arises from a combination of magnetic and thermo-mechanical loads, as well as from effects of neutron irradiation. However, even before plasma ignition, a tokamak is loaded by its own weight, and also its vacuum vessel is loaded by the atmospheric pressure.

First, deformations due to gravity alone are evaluated by imposing the gravitational body force on all the components while fully constraining the displacements at the bottom of the four supporting legs of the tokamak. The bulk of the tokamak structure consists of stainless steel. From the total volume of the structure of 8.55 m^3 and the density of 304SS steel of 8,000 kg/m^3, we estimate the total weight of steel parts of 68.4 tons. Copper windings with the total volume of 2.96 m^3, assuming the weight of solid copper (density 8,960 kg/m^3) adds 26.5 tons to the weight of the tokamak. The poloidal field coils are supported inside the chamber whereas the toroidal field coils run around the external surface of the vacuum vessel. The carbon tiles (with density of 2,260 kg/m^3) constitute a small fraction of the total weight of the device; the total volume of carbon components is 1.78 m^3, contributing 4.03 tons to the mass of the device. The total mass of the modelled tokamak is therefore about 98.9 tons, while the estimated total mass of the real device is close to 110 tons.

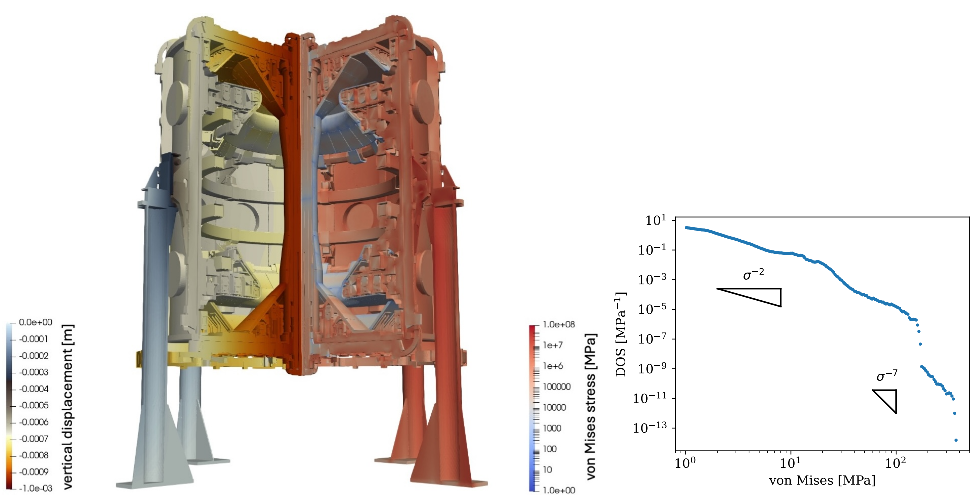

Figure 6. Vertical downward displacement, in relation to the foundation, of the entire tokamak structure (left half of the tokamak) and the von Mises stress resulting from gravitational loading (right half of the structure, on a logarithmic colour scale). Highest values of displacements and stress are reached at brackets where the vessel transfers its weight onto the supporting pillars, where the von Mises stress reaches the maximum of ~370 MPa. The *density* of von Mises stress (DOS), i.e. the probability of finding a certain value of stress anywhere in the tokamak structure, computed using the gravitationally loaded FEM of the device, is shown in the right panel. The slopes shown in the insets indicate the approximate exponents of power-law distributions. The power law exponent for the tail part of the density of stress is higher, highlighting the extreme value statistics of high magnitude stress values in the reactor structure.

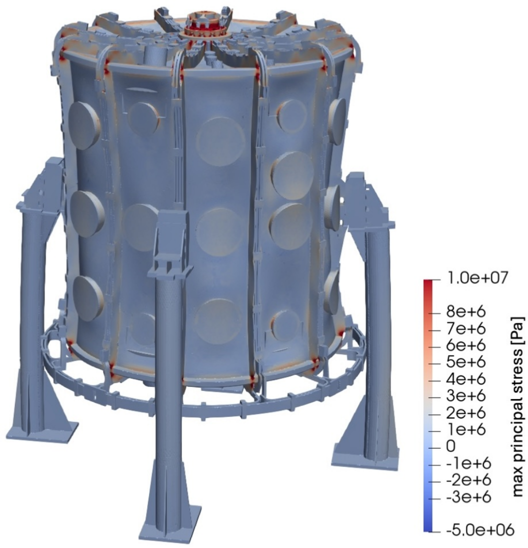

Figure 7. Maximum principal stress values in the tokamak structure if atmospheric pressure is applied to the external surfaces. Deformations shown in the figure are magnified 500-fold to emphasise the deformation pattern of the structure.

The global map of vertical gravitational displacements and the resulting von Mises stress invariant for the static analysis are shown in Fig. 6. The downward displacement of the central column is clearly visible, and the magnitude of this displacement is close to 1 mm, in agreement with observations. The weight of the entire vessel is transferred onto the legs through four supporting brackets, where the highest stress values are recorded. The von Mises stress reaches the value of order of 100 MPa, with a highly localised maximum value close to 300 MPa where the supports are fixed to the side of the vessel. From the values of stress at every tetrahedral element, we can answer the question about the likelihood of finding any particular stress value. We answer it in terms of volume fractions, where the probability of observing the value of stress between σ and $\sigma + \delta\sigma$ is quantified by tallying the volume of all the elements where stress value falls within the σ to $\sigma + \delta\sigma$ bin. We term this quantity the density of stress (DOS), in units of MPa^{-1}. Fig. 6 shows that the majority of the structure is under very modest values of the von Mises stress. The data points at the tail of the distribution, corresponding to the stress value above $\sim$ 100 MPa, all come from the supporting brackets region.

A detailed analysis of effects of external loading also ought to include the effect of atmospheric pressure exerted on the external surfaces of the machine. Applying the pressure of 1 atmosphere, or 0.1013 MPa, to the exterior surfaces produces the stress field illustrated in Fig. 7, where the maximum principal stress is shown as the representative quantity. The figure also shows the magnified inward displacement of the steel structure. The stresses are the highest at the top and bottom rims of the cylindrical vessel. This is to be expected since there the two linear parts of the structure, the walls of the cylinder and the top and bottom plates, are connected at a sharp angle and are stressed by the applied bending moment. The inward displacements of the top and bottom plates are constrained by the central column. The region where the two ends of the central column are in contact with the plates is the second region of high stress concentrations. In absolute terms, the stresses remain fairly low for steel, remaining below 100 MPa. However, it is remarkable that their magnitude is a hundred to a thousand times the applied atmospheric pressure.

The mechanical analysis of gravity and atmospheric pressure effects shows that the stress values are still below the level that would be considered unsafe for the machine, but are at the same time high enough to warrant attention. For example, materials in a reactor will be exposed to appreciable levels of irradiation and hence will experience radiation creep that is known to be significant for applied stresses in the 100 MPa range [20].

6 Summary and conclusions

We conclude by assessing the implications of the above analysis for modelling a full fusion power plant. The FEM model for a MAST-U tokamak described above involves in excess of 10^8 tetrahedral elements. Taking the 800m^3 plasma volume of ITER as a reference value, and comparing this with the MAST-U plasma volume of 8 m^3, we can infer that a fusion power-generating device of comparable complexity but a hundred times larger would require a 10^{10}-element FEM model to simulate its structure at the same level of spatial resolution.

We also note the implications of the above for engineering programmes on testing and qualification of fusion materials. These programmes still remain relatively imprecise and opinion-based, limiting their value for fusion reactor design studies. The notion of the *density of conditions* introduced above, defined in the form of the density of stress in Fig. 6, enables specifying the operating conditions for which materials need to be tested, at a better level of exactness, both in terms of the definition of the range of relevant parameters as well as in terms of the frequency of occurrence of such conditions.

Acknowledgements

This work has been carried out within the framework of the EUROfusion Consortium, funded by the European Union via the Euratom Research and Training Programme (Grant Agreement No 101052200 — EUROfusion). The work was also funded by the UK Fusion Futures and the EPSRC Energy Programmes (grant number EP/W006839/1). We gratefully acknowledge using resources provided by the Cambridge Service for Data Driven Discovery (CSD3) and by Cineca (Marconi).

References

[1] S. Meschini, F. Laviano, F. Ledda *et al.*, *Review of commercial nuclear fusion projects*, Frontiers in Energy Research **11**, 1157394 (2023) https://doi.org/10.3389/fenrg.2023.1157394

[2] F. M. Poli, *Integrated Tokamak modeling: When physics informs engineering and research planning*, Phys. Plasmas **25**, 055602 (2018) https://doi.org/10.1063/1.5021489

[3] L. M. Giancarli *et al.*, *Overview of recent ITER TBM Program activities*, Fusion Engineering and Design **158**, 111674 (2020) https://doi.org/10.1016/j.fusengdes.2020.111674

[4] A. A. Kaptanoglu, G. P. Langlois, M. Landreman, *Topology optimization for inverse magnetostatics as sparse regression: Application to electromagnetic coils for stellarators*, Computer Methods in Applied Mechanics and Engineering **418**, 116504 (2024) https://doi.org/10.1016/j.cma.2023.116504

[5] B. W. Spencer, W. M. Hoffman, S Biswas *et al.*, *Grizzly and BlackBear: Structural Component Aging Simulation Codes*, Nuclear Technology **207**, 981 (2021) https://doi.org/10.1080/00295450.2020.1868278

[6] A. Sykes, R. J. Akers, L. C. Appel *et al.*, *First results from MAST*, Nuclear Fusion **41**, 1423 (2001) https://doi.org/10.1088/0029-5515/41/10/310

[7] J. Milnes, N. Ben Ayed, F. Dhalla *et al.*, *MAST Upgrade – Construction Status*, Fusion Engineering and Design **96-97**, 42 (2015) https://doi.org/10.1016/j.fusengdes.2015.03.002

[8] W. Morris *et al.*, *MAST upgrade divertor facility: a test bed for novel divertor solutions*. IEEE transactions on plasma science **46**, 1217–1226 (2018) https://doi.org/10.1109/TPS.2018.2815283

[9] Coreform Cubit (Version 2023.11) [Computer software]. Orem, UT: Coreform LLC. http://coreform.com

[10] C. J. Permann *et al.*, *MOOSE: Enabling massively parallel multiphysics simulation*. SoftwareX **11**, 100430 (2020) https://doi.org/10.1016/j.softx.2020.100430

[11] S. L. Dudarev, P.-W. Ma, *Elastic fields, dipole tensors, and interaction between self-interstitial atom defects in bcc transition metals*, Physical Review Materials **2**, 033602 (2018) https://doi.org/10.1103/PhysRevMaterials.2.033602

[12] L. Reali, M. Boleininger, M. R. Gilbert, S. L. Dudarev, *Macroscopic elastic stress and strain produced by irradiation*, Nuclear Fusion **62**, 016002 (2022) https://doi.org/10.1088/1741-4326/ac35d4

[13] C. Fausser, A. Puma, F. Gabriel, & R. Villari, Tokamak DT neutron source models for different plasma physics confinement modes. *Fusion Engineering And Design*. **87**, 787-792 (2012) https://doi.org/10.1016/j.fusengdes.2012.02.025

[14] P. Romano, N. Horelik, B. Herman, A. Nelson, B. Forget, & K. Smith, OpenMC: A state-of-the-art Monte Carlo code for research and development. *Annals Of Nuclear Energy*. **82** pp. 90-97 (2015) https://doi.org/10.1016/j.anucene.2014.07.048

[15] Double-down (Version 1.1.0) [Computer software] https://github.com/pshriwise/double-down.git

[16] A. Plompen, O. Cabellos, C. De Saint Jean, M. Fleming, A. Algora, M. Angelone, P. Archier, E. Bauge, O. Bersillon, A. Blokhin, *et al.* The joint evaluated fission and fusion nuclear data library, JEFF-3.3. *The European Physical Journal A*. **56** pp. 1-108 (2020) https://doi.org/10.1007/s10894-021-00299-0

[17] L. Reali, M. R. Gilbert, M. Boleininger, S. L. Dudarev, *Intense γ-Photon and High-Energy Electron Production by Neutron Irradiation: Effects of Nuclear Excitations on Reactor Materials*, PRX Energy **2**, 023008 (2023) https://doi.org/10.1103/PRXEnergy.2.023008

[18] M. Boleininger, S. L. Dudarev, A. E. Sand, E. Martínez, *Volume of a dislocation network*, Physical Review Materials **6.6**, 063601 (2022) https://doi.org/10.1103/PhysRevMaterials.6.063601

[19] M. Boleininger, D. R. Mason, A. E. Sand, S. L. Dudarev, *Microstructure of a heavily irradiated metal exposed to a spectrum of atomic recoils*, Scientific Reports **13**, 1684 (2023) https://doi.org/10.1038/s41598-022-27087-w

[20] F. Onimus *et al.*, *Irradiation Creep in Materials*. In: Comprehensive Nuclear Materials. 2nd edition, vol. 1 (2020) pp. 310–366. https://doi.org/10.1016/B978-0-12-803581-8.11645-5